Biomicrofluidics ARTICLE pubs.aip.org/aip/bmf

Non-invasive measurement of wall shear stress in microfluidic chip for osteoblast cell culture using improved depth estimation of defocus particle tracking method

Cite as: Biomicrofluidics **18**, 054114 (2024); doi: 10.1063/5.0226294
Submitted: 30 June 2024 · Accepted: 15 October 2024 ·
Published Online: 24 October 2024

Hein Htet Aung,[1,a)] Phattarin Pothipan,[2,b)] Jirasin Aswakool,[1,c)] Siraphob Santironnarong,[3,d)] Rungrueang Phatthanakun,[4,e)] Visarute Pinrod,[5,f)] Thanakorn Jiemsakul,[5,g)] Wares Chancharoen,[1,h)] and Aekkacha Moonwiriyakit[2,h)]

AFFILIATIONS

[1]Laboratory of Artificial Intelligence and Innovation in Medicine (AIIM), Princess Srisavangavadhana College of Medicine, Chulabhorn Royal Academy, 906 Kampangpetch 6 Rd., Talat Bang Khen, Lak Si, Bangkok 10210, Thailand
[2]Chakri Naruebodindra Medical Institute, Faculty of Medicine Ramathibodi Hospital, Mahidol University, 111 Suwannabhumi Canal Rd, Bang Pla, Bang Phli District, Samut Prakan 10540, Thailand
[3]Defence Technology Institute, Office of the Permanent Secretary of Defence (Chaengwattana) 7th Floor, 47/433 Moo 3, Ban Mai, Pak Kret, Nonthaburi 11120, Thailand
[4]Synchrotron Light Research Institute, 111 University Avenue, Muang District, Nakhon Ratchasima 30000, Thailand
[5]National Nanotechnology Center (NANOTEC), National Science and Technology Development Agency (NSTDA), Thailand Science Park, Pathumthani 12120, Thailand

[a)]harry.heinhtet@gmail.com
[b)]phattarin.pot@mahidol.edu
[c)]jirasin.asw@gmail.com
[d)]sirasanti016460818@gmail.com
[e)]rungruang.ems@gmail.com
[f)]visarute.pin@nanotec.or.th
[g)]thanakorn.jie@nanotec.or.th
[h)]**Authors to whom correspondence should be addressed:** wares.cha@cra.ac.th. **Tel.:** +66625766718 and aekkacha.moo@mahidol.edu. **Tel.:** +6628395206.

ABSTRACT

The development of a non-invasive method for measuring the internal fluid behavior and dynamics of microchannels in microfluidics poses critical challenges to biological research, such as understanding the impact of wall shear stress (WSS) in the growth of a bone-forming osteoblast. This study used the General Defocus Particle Tracking (GDPT) technique to develop a non-invasive method for quantifying the fluid velocity profile and calculated the WSS within a microfluidic chip. The GDPT estimates particle motion in a three-dimensional space by analyzing two-dimensional images and video captured using a single camera. However, without a lens to introduce aberration, GDPT is prone to error in estimating the displacement direction for out-of-focus particles, and without knowing the exact refractive indices, the scaling from estimated values to physical units is inaccurate. The proposed approach addresses both challenges by using theoretical knowledge on laminar flow and integrating results obtained from multiple analyses. The proposed approach was validated using computational fluid dynamics (CFD) simulations and experimental video of a microfluidic chip that can generate different WSS levels under steady-state flow conditions. By comparing the CFD and GDPT velocity profiles, it was found that

the Mean Pearson Correlation Coefficient is 0.77 (max = 0.90) and the Mean Intraclass Correlation Coefficient is 0.66 (max = 0.82). The densitometry analysis of osteoblast cells cultured on the designed microfluidic chip for four days revealed that the cell proliferation rate correlates positively with the measured WSS values. The proposed analysis can be applied to quantify the laminar flow in microfluidic chip experiments without specialized equipment.

 https://doi.org/10.1063/5.0226294

I. INTRODUCTION

Recently, fields such as biology, medicine, and pharmacy have shown increased interest in the application of microfluidic devices to research and development, owing to these devices' potential for size and cost reduction, and integrating multiple functions into a single platform.[1] A major advantage of microfluidics is the ability to replicate complex cell environments and carry out precise manipulations for improved analysis, such as immobilization, sorting, stimulation, and perturbation.[2] The adoption of polydimethylsiloxane (PDMS) materials can ensure the successful application of microfluidic technology in cell culturing. The PDMS serves as a key enabler, allowing the precise recreation of specific environmental conditions conducive to the growth of cells such as myoblast or osteoblast cells.[3–5] The unique physical properties of PDMS, characterized by resilience and stress resistance, make it suitable for establishing controlled cell culture environments. To ensure their optimal growth and functionality, different cell types require different culturing conditions, such as specific nutrient availability, spatial confinement, flow rates, and media viscosity within the microfluidic devices. Appropriate culturing is important for optimizing the performance of cells. Specifically for osteoblasts, that is, cells that form bone by secreting its protein matrix, a significant condition for their ideal culture is the presence of fluid-shear stress. Using a specially designed microfluidic device and flow conditions, the fluid-shear stress exerted on the walls, called wall shear stress (WSS), can be predicted and controlled.[6] Osteoblasts thrive under a suitable WSS, exhibiting enhanced density and differentiation compared with static environments. Previous research has shown that the relationship between the osteoblast performance and the WSS is non-linear.[7] Therefore, precise WSS measurements within PDMS-based microfluidic systems are crucial for elucidating osteoblast behavior and refining culture methodologies.

Mechanical stimulation plays an important role in regulating osteoblast homeostasis, including cell proliferation and cell differentiation. The osteoblasts respond to mechanical forces, particularly shear stress resulting from fluid movements, through their cell surfaces. This response involves the activation of mechanoreceptors, including stretch-activated ion channels, integrin-associated proteins, and glycoproteins, leading to the triggering of intracellular signaling pathways.[8] In MC3T3-E1 cells, the fluid-shear stress induces an elongated cell shape and actin filament organization by increasing the expression of cyclooxygenase-2 (COX-2) and c-Fos.[9] Low shear stress (0.1 Pa) promotes cell differentiation by increasing the expression of osteogenesis-related genes (alkaline phosphatase and osteocalcin) and calcium deposition.[10] The release of adenosine triphosphate (ATP) and prostaglandin E2 (PGE2) is induced by shear stress (1.2 Pa).[11] The production of ATP and PGE2 is important for bone remodeling. However, few studies have investigated changes in osteoblast behavior under low-fluid-shear conditions (<0.3 Pa). Owing to the miniscule dimensions of microfluidic systems, it is often challenging to investigate the internal physical properties and dynamics using common measurement methods. Additionally, the microscale environment changes the fluid dynamics compared with what is normally observed at larger scales. For example, the Brownian motion, surface tension effect, and capillarity phenomena are more pronounced at microscale.[12,13]

In microfluidics, the measurement of fluid flow has significantly evolved from basic visualization methods to sophisticated computer vision and sensor-based techniques. Early approaches relied on direct visual observation and dye tracing methods[14] and were gradually replaced by more quantitative techniques such as Particle Image Velocimetry (PIV) and Laser Doppler Velocimetry (LDV) facilitated by advances in high-speed imaging and fluorescent microscopy.[15,16] The integration of microfabricated sensors within microfluidic devices further enhanced the flow monitoring capabilities, allowing for the real-time, *in situ* measurement of various flow parameters.[17] More recently, the application of machine learning and computer vision algorithms has introduced new methodologies in flow analysis, enabling the automated, high-throughput analyses of complex flow patterns.[18] Complementary to measurements, preliminary Computational Fluid Dynamics (CFD) simulations are crucial for understanding fluid behaviors in microfluidic systems. However, validating CFD results with experimental data necessitates capturing and analyzing real-time, three-dimensional data, which presents significant challenges.[19]

Computer vision tools for analyzing and measuring the conditions inside microfluidic devices are a proven method for the noninvasive collection of physical data inside a microfluidic chip and particularly suitable for cell analysis.[18] In recent years, with the advancement of image processing algorithms, the application of Particle Tracking Velocimetry (PTV) has been increasingly becoming more precise. Compared with the PIV technique, PTV can track individual tracer particles in a fluid, offering improved spatial resolution and providing direct measurements of Lagrangian velocities.[20] Additionally, using an appropriate algorithm, the PTV technique can estimate the position of the particle orthogonal to the visual field, determining its depth. In 2021, Barnkob and Rossi[21] proposed an open tool called DefocusTracker, which can estimate the three-dimensional (3D) position of tracer particles and calculate the 3D velocity vectors of particle movement. The DefocusTracker algorithm can estimate the 3D position of tracer particles using images and videos captured from a single camera by utilizing the effect of optical

distortion (defocusing) caused by the particles' relative displacement from the focal plane. This approach is commonly known as general defocusing particle tracking (GDPT) works by comparing the input particle images to a training set of particle images captured at known depths.

There are certain issues with estimating the depths of out-of-focus particles using DefocusTracker or the recent Gaussian kernel-based depth estimator.[22] Although the magnitude of displacement from the focal plane is relatively precise, the displacement direction is inaccurate. Although the direction confusion is often overcome by using specialized equipment such as a cylindrical lens[23] or spherical aberration;[24] an approach to compensate by using the knowledge about the nature of flow (laminar), positioning of the focal plane to filter out errors and only commonly available equipment has been proposed in this paper. In addition, a manual scaling factor must be derived using information from the training set and the refractive index of the medium to convert algorithmically estimated depth values into physical units. The accuracy of the depth measurement is highly dependent on precise refractive index values, as errors in this parameter can significantly affect the resulting physical measurements. The proposed method eliminates the need for this manual scaling, thereby improving accuracy and reducing potential sources of error.

This paper proposes a novel method combining multiple GDPT results from video data captured with the focal plane set on unique depth positions at the center, top, and bottom wall of the flow channel to construct the whole-channel velocity profile in the depth dimension (z axis) and calculate the WSS exerted on the bottom wall. Experiments were conducted using a microfluidic chip designed in a previous study by the authors[25] to investigate the osteoblast cell; a microscope, single camera, tracer particles, and controlled constant flow rate were also used. The proposed method was validated by CFD simulation. It is important to note that, due to the underlying assumptions of the method, the proposed approach can only be applied to laminar flow. To demonstrate the biological results of the developed microfluidic chip, osteoblast cells were cultured on an identical microfluidic chip under constant flow and static conditions, and the WSS dependency of the growth rate was assessed. With the proposed method, the WSS value, which is a crucial parameter in the osteoblast cell culture, can be measured experimentally without complex equipment setup, allowing the optimization of the microenvironment for culturing osteoblast cells or any other cells with WSS dependency in future research.

II. MATERIALS AND METHODS

A. Design and fabrication of microfluidic chip

A hexagonal microfluidic chip designed to mitigate Kármán vortex flow within the microchannel was used for improved cell culturing. This chip was inspired by geometrical design concepts presented in a previous paper.[4] Microchannels with varying dimensions were incorporated into the chip to facilitate experiments on the influence of multiple-WSS profiles on growth rates. In addition to the hexagonal geometry, the proposed design includes three sets of linear microchannels differentiated by their cross-sectional width (large = 1.6 mm, medium = 0.8 mm, and

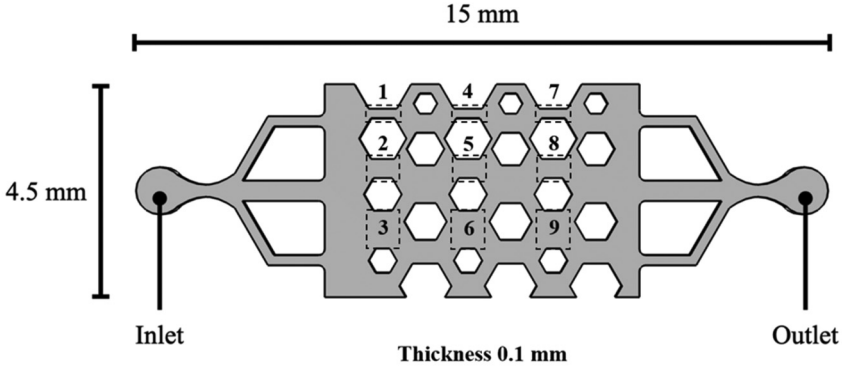

	Upstream	Middle	Downstream
Small	**1** = Small-Upstream (**SU**)	**4** = Small-Middle (**SM**)	**7** = Small-Downstream (**SD**)
Medium	**2** = Medium-Upstream (**MU**)	**5** = Medium-Middle (**MM**)	**8** = Medium-Downstream(**MD**)
Large	**3** = Large-Upstream (**LU**)	**6** = Large-Middle (**LM**)	**9** = Large-Downstream (**LD**)

FIG. 1. Multi-WSS microfluidic chip model and illustration of regions of interest (ROIs) and labeling.

small = 0.4 mm). In each set, there are three microchannels, amounting to a total of nine microchannels, with an identical depth of 0.1 mm fabricated on a single microfluidic chip. As shown in Fig. 1, each region of interest (ROI) can be identified by its width and relative position to inlet/outlets. This single-chip, multi-region design provides a cost-effective solution and reduces the inter-trial variability for biological experiments.

The chip design was created using computer-aided design (CAD) software, enabling high-precision fabrication down to the micrometer and sub-micrometer scales. The COMSOL Multiphysics (COMSOL Inc., USA) software for CFD analysis was used to optimize the microfluidic chip design. The design implements WSS in the range of 90–210 mPA under a flow rate of 50 μl/min. The WSS range was selected to ensure that the cell culture experiment revealed the effect of WSS on the growth rate without causing cell death and detachment.[26] Figure 1 shows the image of the final design of the microfluidic chip with labels for the inlet and outlet used in the simulation. After design optimization, the microfluidic chip was fabricated through a process called soft lithography. This technique involves creating an epoxy master mold using a photomask, photocurable epoxy, and ultraviolet (UV) light. Using the master mold, the final polydimethylsiloxane (PDMS) microfluidic chips were cured in a temperature-controlled oven. The PDMS was selected for its optical clarity, flexibility, and biocompatibility. The cured PDMS was drilled for inlet and outlet attachments and then bonded on a glass slide using oxygen plasma. The fabricated chips were used for experimental video recording and cell culturing. A more detailed description of the fabrication process can be found in the literature[25] and in PDMS fabrication in the supplementary material.

B. CFD analysis for velocity profile and WSS

The numerical analysis of the culture medium or fluid flowing in the microfluidic chip was conducted using COMSOL Multiphysics to solve the Navier–Stokes equation through the finite element method (FEM). Water with a constant density of 1009 kg/m^3 and dynamic viscosity of 0.93 mPa s was selected as the fluid medium. A fully developed flow with a steady flow rate of 20 μl/min was applied to the inlet of the microfluidic chip. A constant pressure of 101 325 Pa was specified both at the inlet and outlet. Second order discretization of pressure and velocity was used to minimize the numerical diffusion and improve accuracy. To select an appropriate turbulence model, the estimated Reynolds number (Re) was calculated for various cross sections corresponding to each ROI, as follows:

$$\mathrm{Re} = \frac{\rho v D}{\mu}, \tag{1}$$

where ρ°, v, and μ are the density (kg/m^3), velocity (m/s), and dynamic viscosity of water (Ps s), respectively; D is the hydraulic diameter (m) defined as $D = \frac{2wh}{(w+h)}$; and w and h are the width (m) and cross-sectional height (m) of the microfluidic channel. Using the definition of flow rate Q (μl/min) and hydraulic diameter D (m), the Reynolds number can be calculated as follows:

$$\mathrm{Re} = \frac{\rho\left(\frac{Q}{wh}\right)\left(\frac{2wh}{w+h}\right)}{\mu} = \frac{2\rho Q}{(w+h)\mu}. \tag{2}$$

The maximum Reynolds number was calculated for regions with the smallest cross-sectional perimeter, that is, regions SU, SM, and SD in Fig. 1, and the obtained value is 0.036, which is below the critical Re of 2300 for internal flow. Therefore, laminar flow is expected, and the laminar model was selected in this study.

The microfluidic chips used in this study consisted of glass and PDMS. To simulate the hydrophobic behavior of flow over PDMS, the Navier slip wall boundary condition was applied to the PDMS walls, while the no-slip wall boundary condition was applied everywhere else. The Navier slip applies a friction force as follows:

$$F_{fr} = -\frac{\mu}{\beta} u_{\tan g}, \tag{3}$$

where μ is the dynamic viscosity of water (Pa s); β is the slip length (μm); $u_{\tan g}$ is the tangential velocity at the wall (m/s); and its magnitude can be calculated as $u_{\tan g} = u - (u \cdot n_{\mathrm{wall}})n_{\mathrm{wall}}$. Chun *et al.*[27] conducted numerical analysis on the flow between the PDMS and glass and found that the slip length is a function of the fluid's pH value and pressure gradient. In this study, the slip length was selected based on the chart of Chun *et al.*,[27] where the pressure gradient is determined beforehand through no-slip wall computation. Simulations were conducted with both no-slip condition and wall slip on PDMS to compare with experimental measurements.

C. Experimental setting using bright-field microscopy for GDPT analysis

The Nikon TS2 bright-field microscope (Nikon Instruments Inc., Japan) with the objective lens set at 10× magnification and a Canon EOS R camera (Canon Inc., Japan) mounted on the side port was used to record video of the fluid flow within the microchannels, as shown in Fig. 2(a). The fluid flow was visualized under the microscope using Sigma-Aldrich 42922 microparticles (Sigma-Aldrich®, USA), which are 3-μm-diameter polystyrene pigment, as the tracer particles. The de-ionized water and tracer particle mixture was prepared at a concentration of 1:5000 by volume to ensure sufficient dispersion and reduce the overlapping of particles. This ratio minimizes the particle per pixel (PPP) value to reduce errors in GDPT.[28] Using a syringe pump (LongerPump: LSP01-1C, Longer Precision Pump Co. Ltd., UK) connected to the chip inlet, the particle and water mixture were pumped into the microfluidic chip at a constant flow rate of 20 μl/min. The low flow rate ensured that the video recording could capture the trajectories of the fastest-moving particle for at least seven consecutive frames. An ultrasonic bath was used to remove air bubbles, which can interfere with the flow behavior within the channels. The video was captured in H.264 format at a resolution of 1920 × 1080 pixels with a frame rate of 60 fps. This experimental setup, which is common in biological laboratories, makes the data collection method highly accessible and results in a simple video file. The GDPT method allows for the reconstruction of the

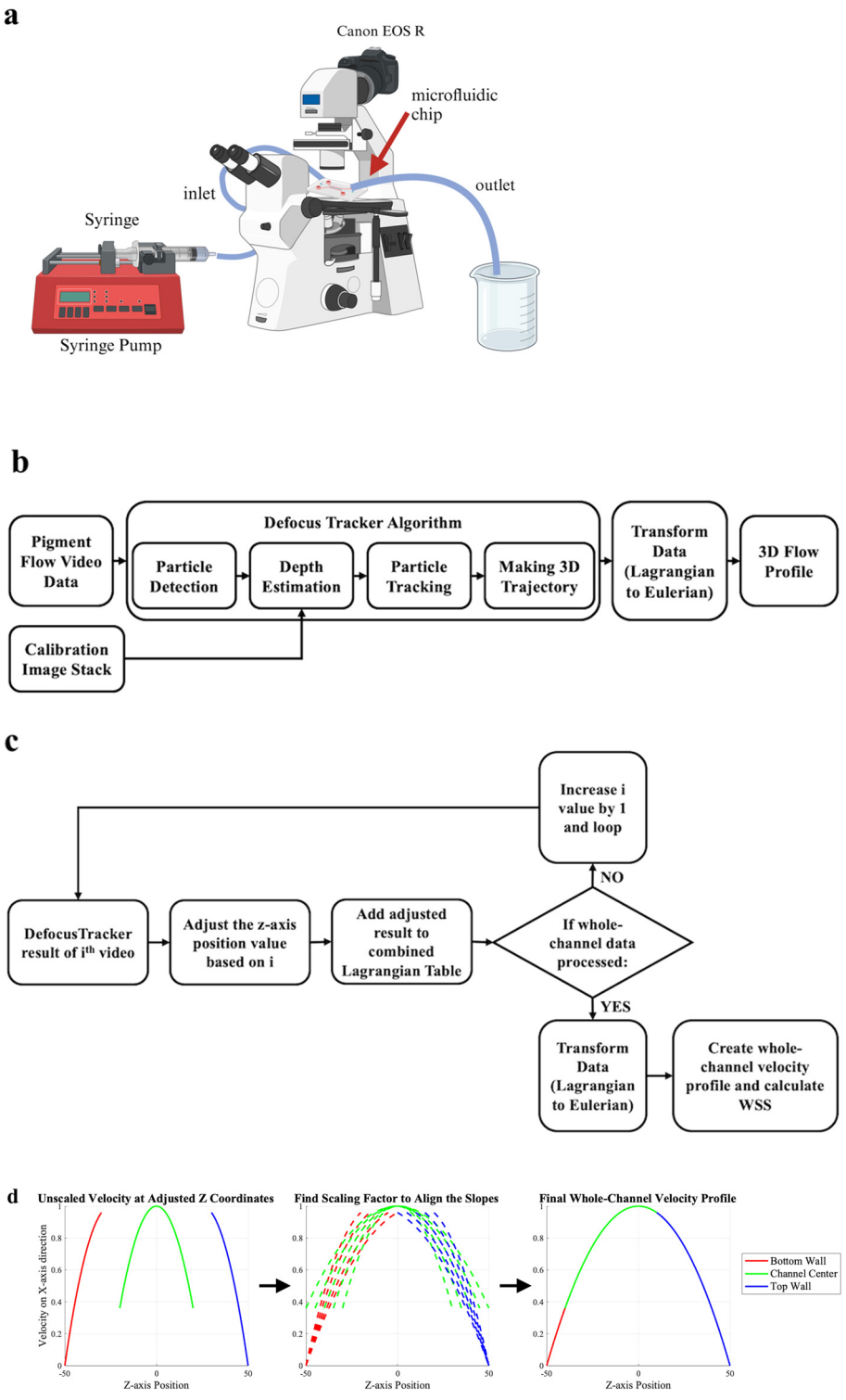

FIG. 2. (a) Illustration of laboratory setup; (b) flow chart of GDPT implementation for generation of 3D flow profile; (c) flow chart of the method for analyzing multiple videos to reconstruct larger 3D velocity profile; and (d) process of calculating a scaling factor and create whole-channel velocity profile.

3D flow field and subsequent calculation of the WSS with respect to the depth (z axis).

D. GDPT analysis for velocity profile and WSS

The DefocusTracker algorithm was implemented in MATLAB using an open-source library[21] to conduct the GDPT analysis. As shown in Fig. 2(b), a calibration stack, that is, a set of images captured at known depth (z axis) values, is necessary to create a "look-up" table for depth estimation. In this study, the calibration stack was created by capturing photos of particles stuck on the glass slide of the microfluidic chip at depth increments of 2 μm. For detailed description of obtaining the calibration stack, see the calibration stack in the supplementary material. Subsequently, the analysis of the particle flow video data was carried out. First, the algorithm identified all 2D positions of every detectable individual particle. Then, the depth of each particle was estimated by calculating the normalized cross correlation with the images in the calibration stack and finding the maximum.[29] By analyzing the two consecutive images using the nearest neighbor approach, the quasi-instantaneous velocity was predicted and a trajectory was defined when a particle remained in the video for more than seven frames.[21]

The DefocusTracker output is a table with each detected particle as a row entry, encompassing a total of nine columns: frame number (fr), spatial coordinates (x, y, and z), displacements (dx, dy, and dz), unique identifier (id), and maximum correlation (cm) value for tracking accuracy. These structured data enable the precise analysis of the particle trajectories and behaviors in three-dimensional space from a Lagrangian perspective. However, to generate a 3D flow profile, the data must be converted into a structured grid from a Eulerian perspective using custom MATLAB code, which can be accessed through the link provided in code availability statement. To convert the velocity from algorithm units (pixel/frame) to physical units (μm/s), a scaling factor is calculated from the experimental parameters. Preliminary analysis revealed that only when the focal plane was set on the center of the microchannel, the measurement exhibited a meaningful trend in the 3D velocity profile. In summary, the in-focus particle had the highest velocity, and the velocity decreased with respect to the magnitude of displacement from the focal plane. The displacement direction had a minor effect on the velocity measurement accuracy. However, when the focal plane is set at the center of the microchannel, it is uncertain whether the tracking results will include the entire depth range of the channel, particularly the velocity of the particles near the top and bottom walls (furthest positions from center).

To ensure that the constructed velocity profile included the fluid flow in the entire depth of the microchannel, multiple videos were recorded. The first video was set to focus on the particles adhering to the glass wall (the side of the microchannel closest to the microscope's objective lens). For each subsequent video recording, the focus plane moved toward the PDMS wall of the microchannel (furthest from the objective lens) by 50 μm. This approach ensures that the fluid flow of the entire 100-μm (0.1 mm) depth range can be captured in three separate video files. As shown in Fig. 2(c), each video was analyzed independently by the DefocusTracker algorithm. Using custom code, the analysis results were combined by adjusting the z axis position of the particles based on the video recording setup (adjustment of 50 μm) to ensure that in-focus planes were fixed to their physical position. After converting the combined results to Eulerian data, a scaling factor that best align the gradients of the adjacent velocity profile is calculated to scale the individual velocity profile from single video analysis, thus bypassing the need for manual scaling. Figure 2(d) demonstrate how the individual velocity profile obtained from multiple video analysis is combined and scaled. The whole-channel velocity profile in the z axis was constructed by integrating the two velocity profiles at both channel walls (top and bottom) and one velocity profile at the channel center. This strategic positioning of the focal plane allows rejection of error caused by direction confusion by eliminating the trajectories that lies outside the physical dimension of the microchannel. As the velocity profile at the center of a laminar flow is symmetrical, the direction confusion does not affect the velocity profile. Each video covered a depth of approximately 80 μm (uncertain owing to the combination of the refractive index of the glass and water). The purpose of the whole-channel velocity profile is to confirm that the flow in the microchannel is a fully developed flow with a velocity profile that does not change along the x axis[30] and to convert the algorithmically estimated depth units to physical units without requiring a manual scaling factor.

From the chip design, the depth of the microchannel is known to be 100 μm. For the combined velocity profile, the depth axis (z axis) is labeled with "0 μm" at the center, "−50 μm" at the PDMS wall, and "+50 μm" at the glass wall of the microchannels. For each ROI defined in Fig. 1, data from three specific DefocusTracker experiments were loaded from ".mat" files in a specified directory. The data of each file were filtered to include only valid particle IDs and normalized for spatial coordinates. The y axis range was restricted to 45%–55% of the total range to focus on the central region of the microchannel, where the velocity and WSS are maximum. As shown in Fig. 2(c), considering that the z axis adjustment is 50 μm, the three results were combined into a single Lagrangian tracking table. By taking the mean velocity of all particles in the z axis binning range, an array was constructed with averaged velocity values in one column and the respective z axis positions (with a constant increment) in another. The z axis velocity profiles from all nine ROIs were visualized, and the formation of fully developed flow was confirmed by comparing the velocity profiles generated at different x axis ranges in the preliminary analysis.

After confirming that the algorithmically measured flow of the microchannel was fully developed flow, the calculation of the WSS followed. The data from the whole-channel velocity profiles were used to calculate the velocity gradient with respect to the distance from the glass wall for each region. After calculating the velocity gradient $\frac{\partial u}{\partial z}$ in $\frac{\text{mm/s}}{\text{mm}}$ for all nine regions in Fig. 1, and measuring the WSS by GDPT, τ_{GDPT} (mPa) was calculated by multiplying the velocity gradient with the viscosity μ (mPa s) of the fluid, as follows:

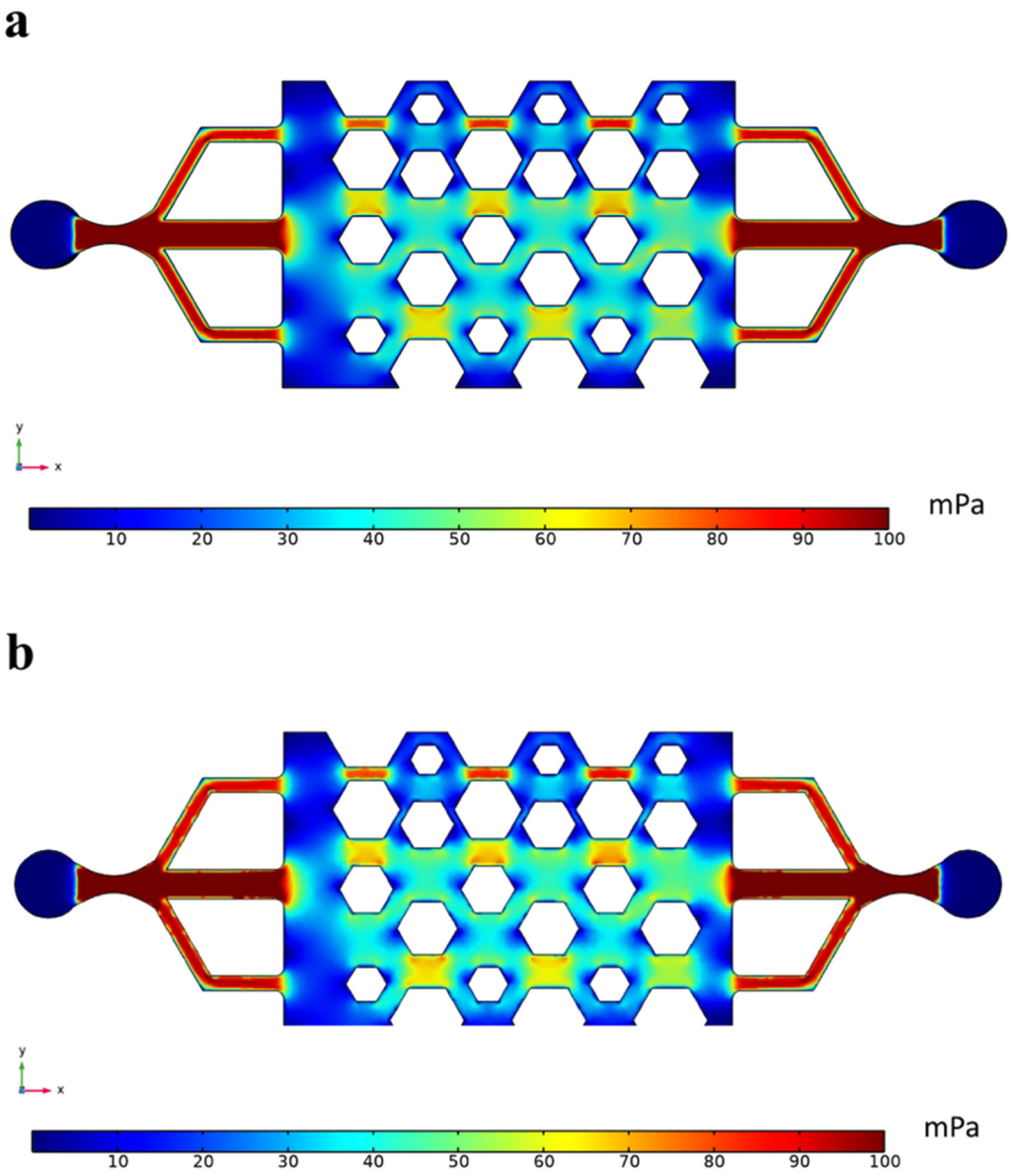

FIG. 3. WSS contour at a flow rate of 20 μl/min for entire microfluidic chip: (a) nonslip condition and (b) wall slip on PDMS.

$$\tau_{\mathrm{GDPT}} = \frac{\partial u}{\partial z} * \mu. \tag{4}$$

The measured WSS values of the nine ROIs were combined into three averaged values based on the channel size of the ROI, effectively calculating the mean WSS value (and standard deviation) for ROIs with small, medium, and large cross sections. The GDPT analysis results were compared with the WSS values obtained from the CFD simulation with the no-slip condition and those obtained from another simulation with the wall-slip condition on the PDMS.

E. Cell culture and analysis of cell growth on multi-WSS

The magnitude of the WSS measured experimentally and that of the WSS obtained from the simulation were expected to have

statistically significant influence on the proliferation rate of the osteoblast cell culture. To confirm this, an osteoblast cell culturing experiment was conducted to analyze the change in the cell densitometry over the culturing period of four days.

The pre-osteoblast cells, namely, MC3T3-E1 subclone4, were cultured in minimum essential medium (MEM) alpha supplemented with 100 U/ml penicillin-streptomycin and 10% fetal bovine serum. The cells were maintained in a humidified incubator at 37 °C with 5% CO_2. Before the cell culture, the microfluidic chip was sterilized by UV exposure and then soaked with 70% ethanol for 15 min. The ethanol was rinsed thoroughly with PBS and then pre-incubated with the culture medium. Next, MC3T3-E1 cells were injected into the microfluidic chip at a density of 8×10^5 cells/ml. After seeding for 24 h, 50 ml of the culture medium, which was supplemented with 10 mM β-glycerophosphate (Sigma-Aldrich), 50 μg/ml ascorbic acid (Sigma-Aldrich), and 100 nM dexamethasone (Sigma-Aldrich), was constantly pumped into the devices using a syringe pump (NewEra-1800) at a flow rate of 50 μl/min (92–211 mPa). A static culture with no resultant WSS was grown as a control, and 200 μl of culture medium was renewed once daily. The cell morphology and images were captured using an inverted microscope (ZEISS AXIO Vert.A1).

To quantify the cell growth using image analysis, photographs of the cell culture in different ROIs of the microfluid chip were captured daily. The cell image was changed to eight-bit to convert the image to gray scale. The background subtraction procedure was adjusted to account for variations in the intensity of transmitted light, with a set radius of 30.0 pixels.[31] The threshold was set to 240 to distinguish regions or objects of interest from the background within an image. Then, the image was converted to binary. The Watershed algorithm was selected to partition the area of the connected cells into separate entities.[32] The selected particles were analyzed and their dimensions were quantified, with the minimum area set to 500 square pixels to exclude artifacts. Then, the outlines of the evaluated regions were obtained.[33] The detail implementation of ImageJ cell counting is described in ImageJ cell count in the supplementary material. The biological data are presented as the mean ± Standard Error of the Mean (SEM). Two-way ANOVA followed by Sidak's posthoc test was used for multiple comparisons. A P-value < 0.05 is considered to indicate a significant difference (GraphPad Prism version 9.0).

III. RESULTS

A. CFD flow analysis and visualization

This study conducted CFD simulations to generate data for comparison with the GDPT measurements, including both the velocity profile and the WSS values. As an initial insight into the performance of the designed microfluidic chip, which produces three different shear stress levels based on the width of the channel cross section, the fluid-shear stress exerted on the glass wall is plotted for the entire chip in Figs. 3(a) and 3(b). Figures 3(a) and 3(b) illustrates the WSS contour generated from the simulation with the no-slip condition and from the simulation with the wall-slip condition on the PDMS wall of the chip (−50 μm), respectively. The contours indicate that the WSS values are similar in ROIs with the same cross-sectional width, confirming that the proposed hexagonal-geometry-based design can generate three different levels of WSS values, with each value repeated three times in a single chip. By comparing the simulation results of the no-slip and wall slip on PDMS conditions, it was found that the WSS exerted on the glass wall was greater for the entire chip in the simulation with the wall slip on PDMS.

Figure 3 shows that regions SU, SM, and SD have the highest WSS, while regions LU, LM, and LD exhibit the lowest WSS. This is consistent with a theoretical approximation where the WSS (τ, mPa) of laminar flow can be estimated[4] by Eq. (5), where w is the width (m) and h is the height (m) of the microfluidic channel cross section, v is the average velocity of the fluid flow (m/s), μ is the dynamic viscosity of water (Pa s), and Q is the flow rate (μl/min),

$$\tau = \frac{6v\mu}{h} = \frac{6Q\mu}{wh^2}. \tag{5}$$

This equation, an analytical expression of Poiseuille flow between two infinite parallel plates, indicates that the WSS is inversely proportional to the width and square of the height of the region's cross section. Through CFD, the chip design was confirmed to contain microchannels with WSS inversely proportional to the channel width and with each WSS level repeating in three independent locations.

B. GDPT results

By conducting single video analysis [Fig. 2(b)] on the video where the focal plane is at the center of the microchannel, the 3D flow profile was constructed. Figure 4 shows the 3D velocity

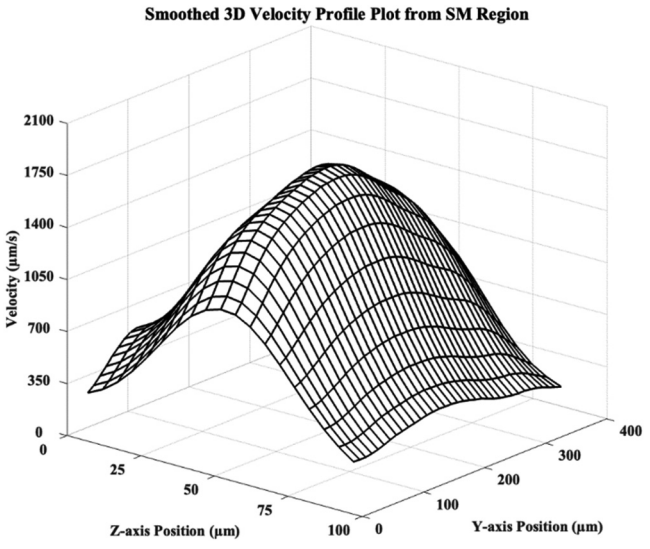

FIG. 4. 3D flow profile constructed from single video recorded in the SM region.

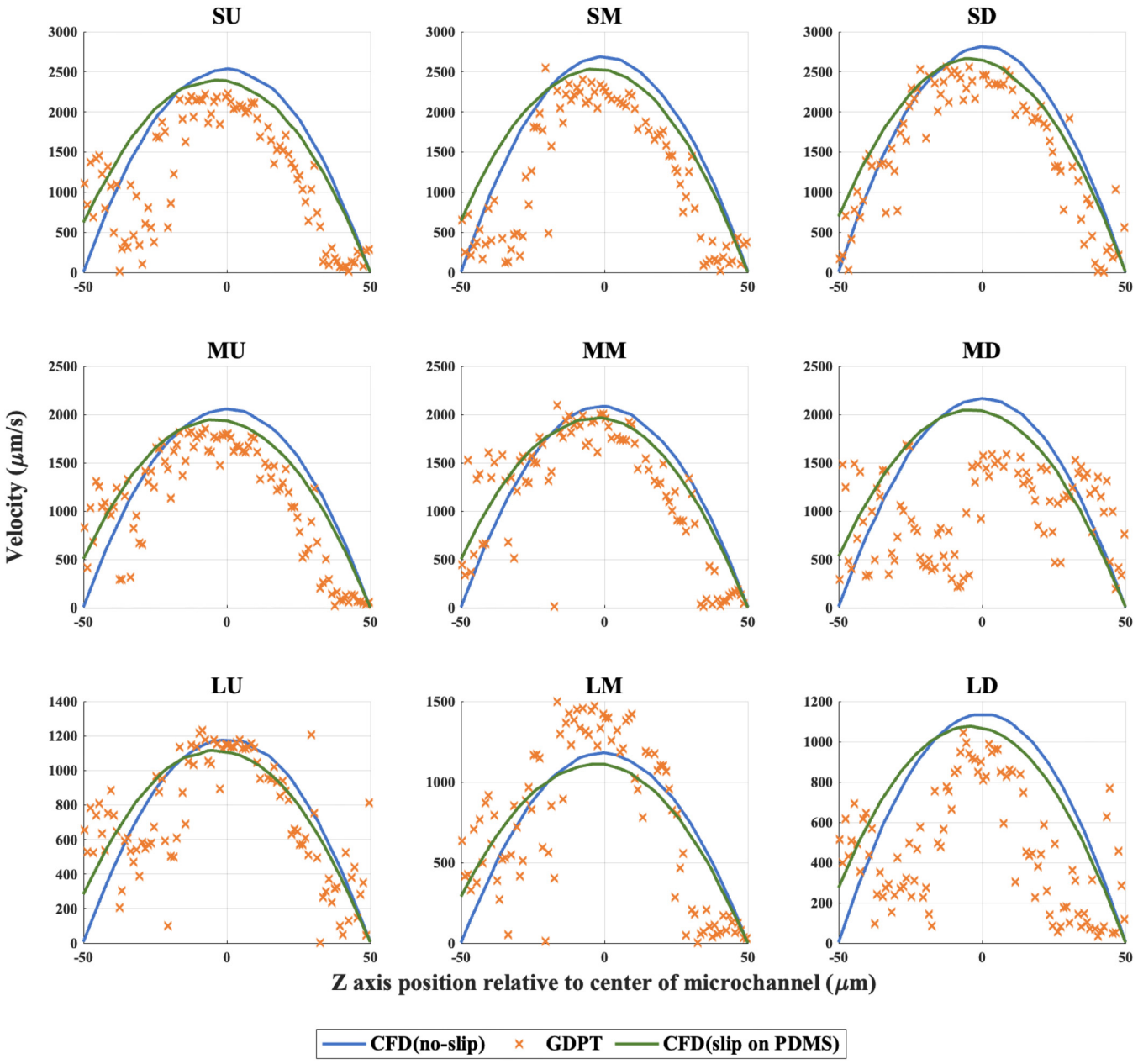

FIG. 5. Velocity (in the x-direction) profile comparison for nine different chip regions. For each region, the velocity is plotted against the *z* axis position (relative distance from the channel center). The CFD simulation results obtained with the wall slip on PDMS (green) and without the wall-slip conditions (blue) are compared with the GDPT results (orange).

profile from the SM region of the microfluid chip. The plot was smoothed using a Gaussian filter with a variance of $1\,\mu m^2$ to reduce noise. The velocity profile of the video, focusing on the center of the microfluidic chip, shows that the flow is fully developed laminar flow, and the maximum velocity magnitude is close to that of the simulation results. This confirms that the velocity scaling factor was correctly calculated from the experimental parameters. However, because the physical unit conversion of the depth (z axis) value is uncertain, a physically relevant velocity gradient and the WSS value cannot be calculated from a single

TABLE I. ICC of GDPT compared with CFD (no-slip) and GDPT compared with CFD (wall slip on PDMS).

ROI	ICC of GDPT and CFD (no-slip)	ICC of GDPT and CFD (wall slip on PDMS)	Note
SU	0.53	0.49	
SM	0.62	0.53	
SD	0.82	0.62	
MU	0.68	0.74	
MM	0.71	0.74	
MD	0.00	−0.11	Outlier
LU	0.67	0.67	
LM	0.73	0.66	
LD	0.21	0.16	Outlier

TABLE II. PCC of GDPT compared with CFD (no-slip) and GDPT compared with CFD (wall slip on PDMS).

ROI	PCC of GDPT and CFD (no-slip)	PCC of GDPT and CFD (wall slip on PDMS)	Note
SU	0.74	0.71	
SM	0.87	0.66	
SD	0.90	0.72	
MU	0.78	0.89	
MM	0.75	0.85	
MD	0.12	0.02	Outlier
LU	0.67	0.69	
LM	0.77	0.79	
LD	0.49	0.54	Outlier

analysis. To construct a more physically accurate whole-channel velocity profile and calculate the WSS value, the integration of multiple results was used.

C. Validation of GDPT with CFD results

By following the method outlined in Fig. 2(c) and selecting the appropriate video files, the velocity profile of the entire channel in the z axis was constructed. The measured velocity profiles and simulated (CFD) velocity profiles were compared for validation. For each region, the velocity profiles were determined by first converting the Lagrangian data tables (GDPT output) into Eulerian grids through a process known as binning. This transformation allows for the integration of particle tracking information into a structured format that aligns with the Eulerian nature of CFD analysis. Subsequently, the data were reduced to one-dimensional profiles by averaging the x-direction velocity across the x axis, at the center of the y axis, and then binned along the z axis in 1 μm increments, plotting the velocity in the x axis direction as a function of the position in the z axis.

In Fig. 5, the whole-channel velocity profiles are compared among the GDPT (orange), simulation with the wall-slip condition on the PDMS side (green), and simulation without the wall-slip condition (blue). To account for the different behaviors of glass and PDMS, which has less friction, a separate simulation with the wall-slip condition on the PDMS side (−50 μm) was included in the comparison. The velocity profile trend of the experimental results from the medium and large channel shows that the velocity does not reach zero on the PDMS side of the microchannel. This is attributed to noise (overlapping particles) or a difference in the coefficient of friction between the glass and PDMS. The comparison of the results obtained by the GDPT to the CFD results confirms that the flow was fully developed in all nine regions. The low quality of the input video data causes higher noise in the GDPT results in the MD and LD regions and the deformities in the velocity profile can be observed. Additionally, the result from LM region shows higher velocity than simulation results. This is attributed to the unusually high number of high velocity trajectories from the GDPT analysis of the video with the focal plane set in the center of the channel.

To quantify the similarity between the CFD results and the GDPT measurements, the Intraclass Correlation Coefficient (ICC) and Pearson Correlation Coefficient (PCC) were calculated.[34,35] In Table I, for all nine ROIs in Fig. 1, the ICC between the GDPT measurement and the CFD with the no-slip condition is presented in column 2. The ICC between the GDPT measurement and the CFD with the PDMS wall-slip condition is presented in column 3 for each of the nine ROIs. Similarly, the PCCs among the GDPT, simulation with the no-slip, and simulation with the PDMS wall slip are presented in Table II. Excluding the outlier data, the ICC with a mean of 0.66 indicates that the measurement has moderate to good reliability. The PCC with a mean of 0.77 indicates a strong relationship between the CFD data and the measurements. The outliers were selected based on the low quality of the raw video input data and excluded from calculating the mean PCC and ICC.

The WSS for the observed velocity data was calculated using Eq. (4). Velocity data with respect to the z axis (depth) were obtained using the DefocusTracker algorithm. The shear stress value at the boundary of the fluid and glass (bottom) wall is a measurement of interest to osteoblast research. Therefore, the shear stress value at the bottom wall (the maximum measurable WSS) was calculated. The velocity data near the glass wall exhibited considerable noise; thus, data points within 10 μm of the wall were excluded from the analysis. To reduce the influence of noise in the calculation of the velocity gradient, a 15 μm gap was set between the positions where data points were selected. The velocity gradient was calculated taking the averaged velocity of five data points nearest to the +40 μm position along the z axis and five data points nearest the +25 μm position. The corresponding wall shear stress (WSS) was then derived from this gradient. The shear stress values calculated from the GDPT measurements (orange) are presented in Fig. 6, along with the WSS values obtained from the simulation with the wall slip on the PDMS side (green) and no-slip condition (blue). Overall, the WSS value calculated based on the GDPT measurements exhibits changes based on the channel size, similar to the CFD results. The WSS measurements from

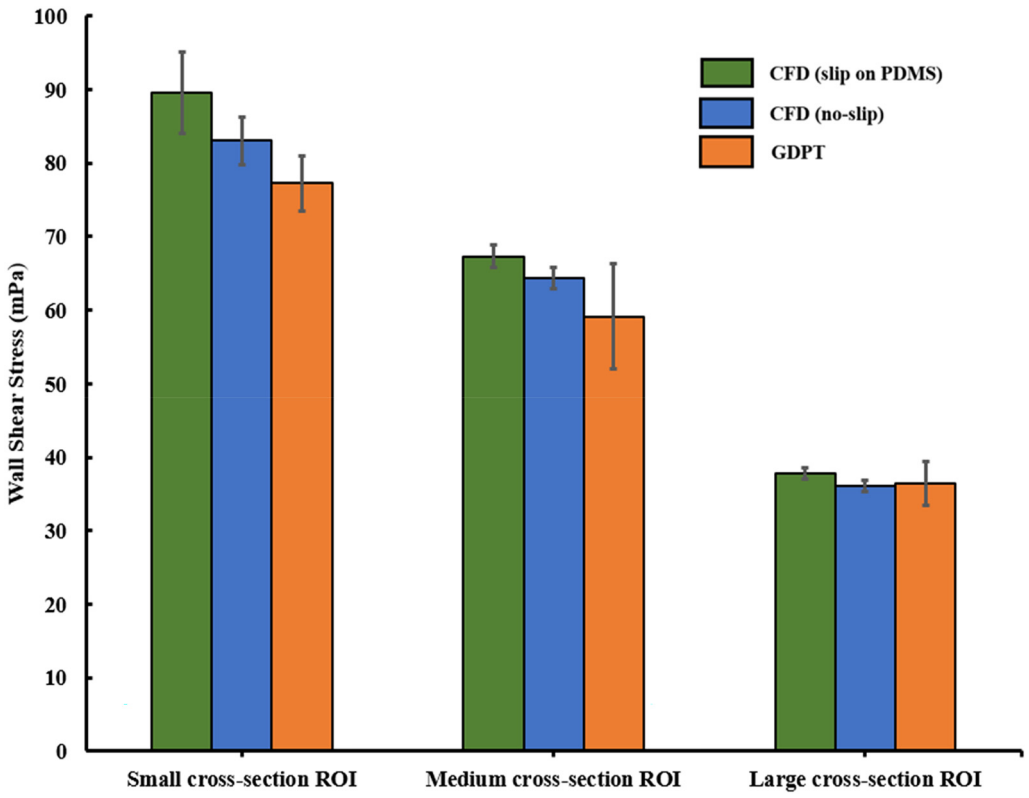

FIG. 6. Bar chart of WSS comparison among GDPT results (orange), simulation with slip on PDMS (green), and simulation with no-slip condition (blue), plotted for each microchannel set with different ROIs.

microchannels with the same cross-sectional width obtained similar values, and the design of the microfluidic chip could generate three different WSS levels. The WSS values of the small-cross-sectional channels (SU, SM, and SD) are the highest and are labeled as the "High WSS" region for the osteoblast culturing experiment. The medium cross-sectional channels (MU, MM, and MD) and large cross-sectional channels (LU, LM, and LD) are labeled as the "medium WSS" region and "low WSS" region, respectively, based on their mean WSS values. The observed discrepancies were caused by the quality of the raw video data, and lower spatial resolution of the data points used to calculate the velocity gradient in the experimental data compared to the simulation.

D. Osteoblast proliferation under multiple WSS

Bones are continuously exposed to a wide range of shear stress from low levels caused by blood infiltration to high levels during exercise. To validate the osteoblast culture in multiple-WSS devices, the MC3T3-E1 cells-on-the-chip were cultured under conditions of either static or steady flow. The WSS intensity at a flow rate of 50 μl/min was determined by CFD as described in Appendix B. Through CFD simulation and experimental measurement, it was confirmed that the chip design has high WSS, medium WSS, and low WSS in three microchannel sets, with three independent regions in each set. In Fig. 1, each ROI row can be identified as a single set of microchannels with a similar WSS level. This allows for the biological experiment to have three independent observations for each level of WSS magnitude on a single microfluidic chip.

After incubating for four days, cells in the static condition exhibited a polygonal and round-shape, while under medium and high WSS, the cells had a more elongated shape, as shown in Figs. 7(a)–9(a). The ratio of (cell count on target date)/(cell count on day 0) was calculated to quantify the normalized proliferation rate. Additionally, the biological experiment was repeated at least five times to reduce the effect caused by difference in initial condition. In fact, cells exposed to medium WSS (165 mPa) and high WSS (211 mPa) exhibited a marked increase in proliferation compared with those under the static condition in Figs. 8(b) and 9(b). A significant elevation of cell density was observed on days 3 and 4, and the effect was WSS-dependent. However, cells exposed to low WSS (92 mPa) only exhibited a slight increase of cell proliferation on day 4, as

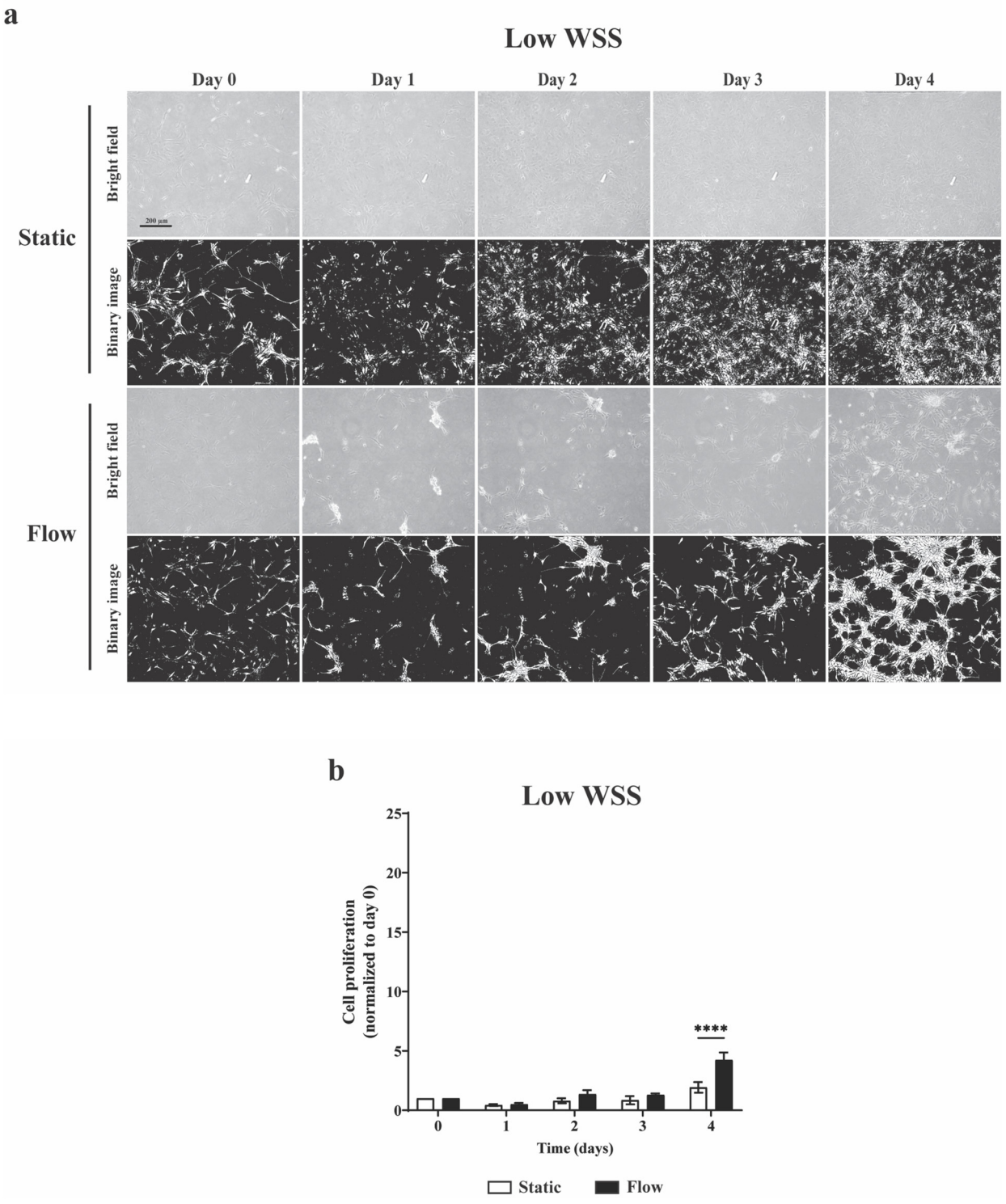

FIG. 7. Effect of low WSS on osteoblast proliferation. (a) Representative images from day 0 to day 4 (inverted microscope, 10×; scale bar = 200 μm). (b) Quantitative analysis of proliferation under medium WSS (mean ± SEM; —five to six experiments; *P < 0.05, **P < 0.01, ****P < 0.0001; two-way ANOVA, Sidak's posthoc).

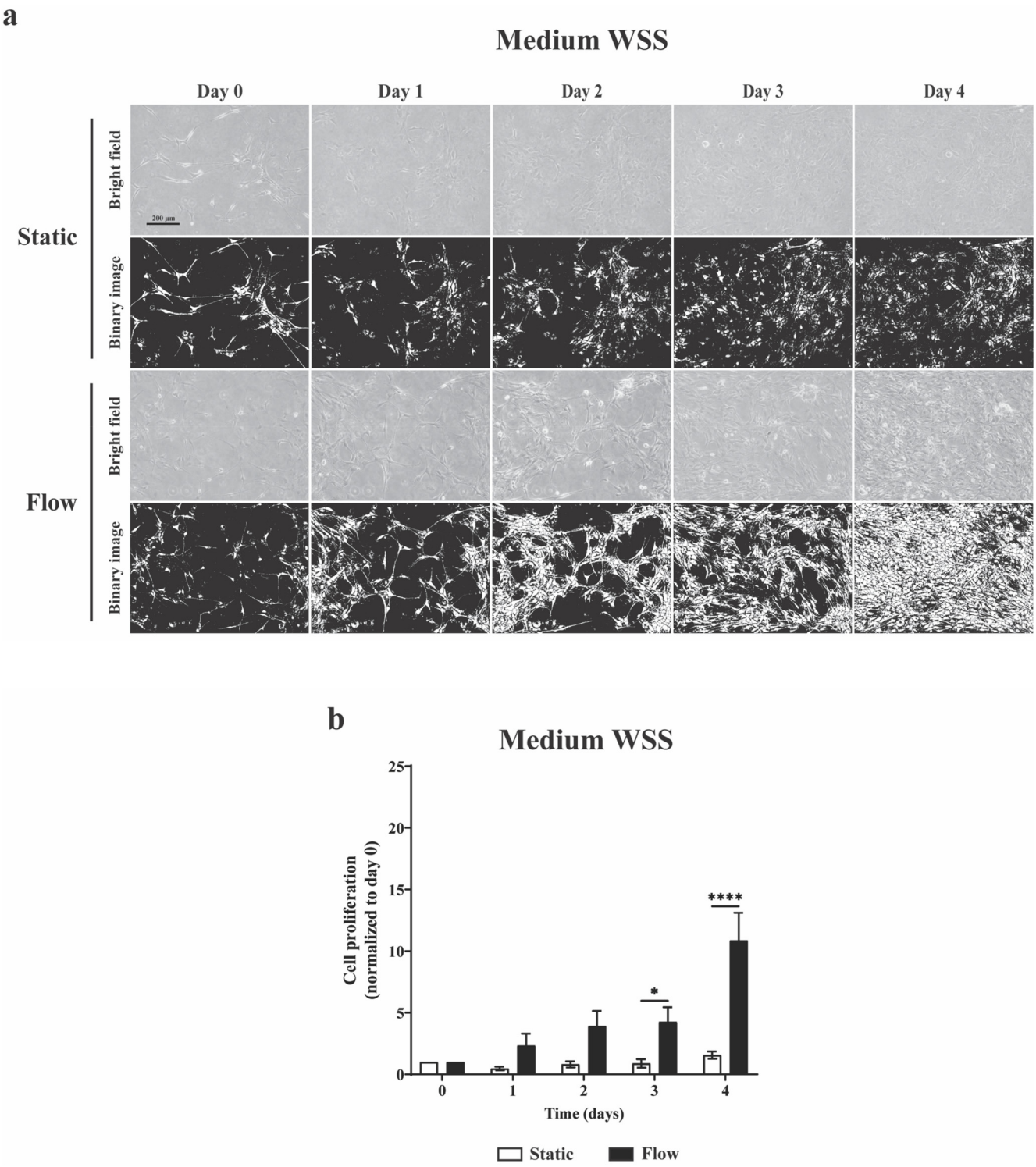

FIG. 8. Effect of medium WSS on osteoblast proliferation. (a) Representative images from day 0 to day 4 (inverted microscope, 10×; scale bar = 200 μm). (b) Quantitative analysis of proliferation under medium WSS (mean ± SEM; —five to six experiments; *P < 0.05, **P < 0.01, ****P < 0.0001; two-way ANOVA, Sidak's posthoc).

shown in Fig. 7(b). Therefore, these results suggest that MC3T3-E1 cells-on-the-chip recapitulate the osteoblast in response to WSS that activates cell proliferation in the magnitude-dependent manner.

This study elucidated the differential growth of osteoblasts, which depends on the degree of shear stress (ranging from 92 to 211 mPa). The findings reveal that the level of WSS enhanced the cell proliferation in a magnitude-dependent manner. The proliferation rate greatly increased both for medium (165 mPa) and high (211 mPa) WSS. The results agree with those obtained by other studies, which demonstrated that fluid-induced shear stress stimulates cell proliferation.[36–38] The osteoblast proliferation is affected even with low WSS (92 mPa). This can be explained by the WSS intensity being in the physiological range of 0.8–3 Pa to which cells in the lacunar–canalicular network are exposed.[39] By comparing the cell proliferation rate between regions with different WSS levels, it was found that the rates differed significantly. The biological results confirm that the measured WSS magnitude has statistically significant influence on the osteoblast cell proliferation rate.

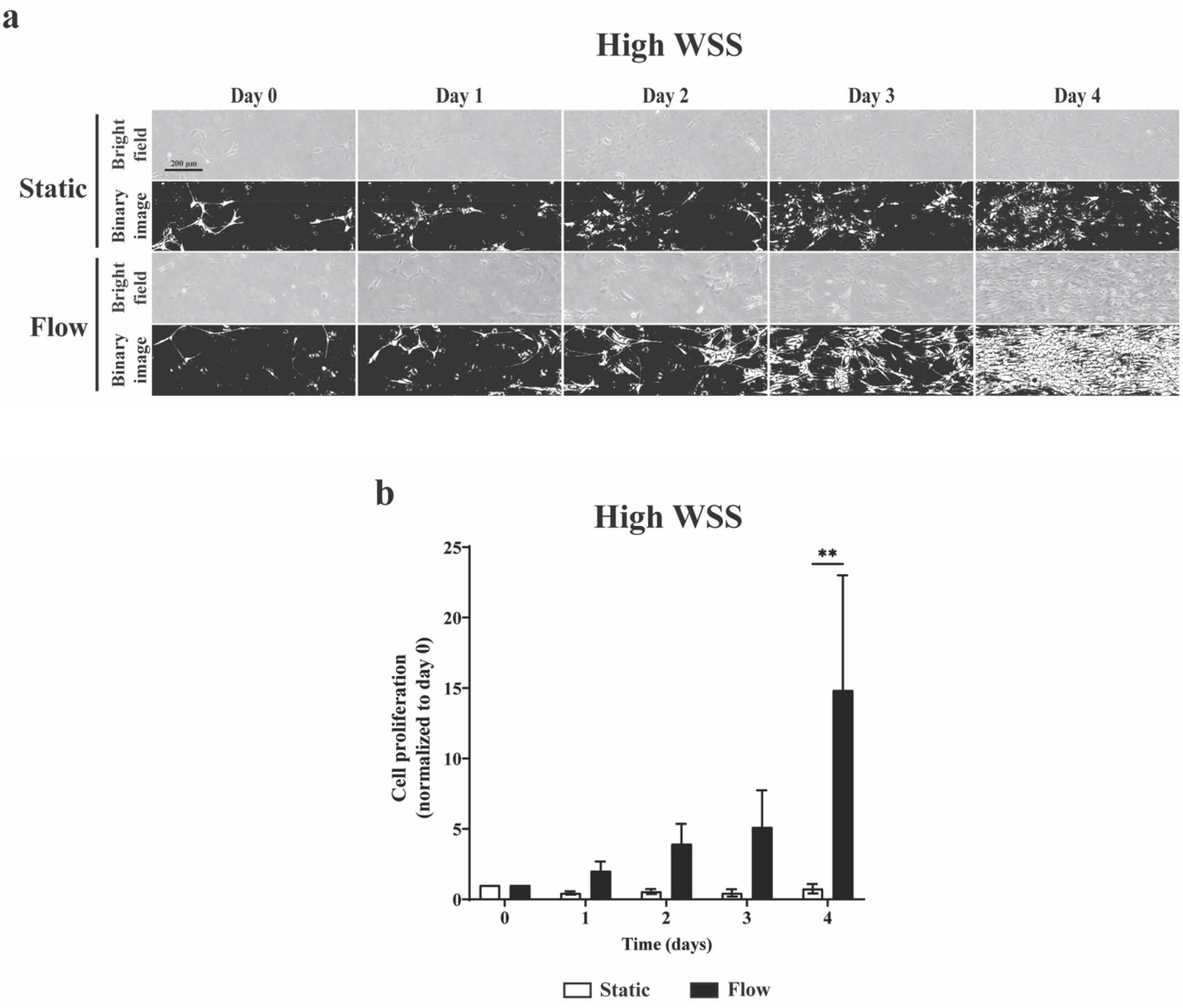

FIG. 9. Effect of high WSS on osteoblast proliferation. (a) Representative images from day 0 to day 4 (inverted microscope, 10×; scale bar = 200 μm). (b) Quantitative analysis of proliferation under medium WSS (mean ± SEM; —five to six experiments; *P < 0.05, **P < 0.01, ****P < 0.0001; two-way ANOVA, Sidak's posthoc).

IV. DISCUSSION

By combining results from multiple video recordings at different focal plane depth positions, this study developed and validated a novel method for improving the depth estimation and velocity profile construction of fluid flow in microfluidics. The measurements were validated by CFD simulation results obtained through experiments on a microfluidic chip designed for osteoblast cell culture. This microfluidic chip can generate different WSS, categorized as small, medium, and large, depending on the channel width. Each channel with different size had three positions (upstream, middle, and downstream) on the chip. The design concept allowed the data collection of three experimental values in a single run. Therefore, the designed microfluidic chip can be used to run simultaneous replications of different WSS factors and investigate more than one independent repetition in a single run. Additional cell culture experiments revealed that the microfluidic chip can produce controllable multi-shear stress conditions that facilitate different osteoblast cell proliferation rates. Moreover, the impact of fluid shear on cell growth has been reported in many cell types, including osteoblasts,[36] chondrocytes,[37] and mesenchymal stem cells.[38] Using the GDPT approach, this study developed a non-invasive method for monitoring the fluid flow condition and calculated the WSS value without requiring complicated equipment setup. Additionally, by integrating results from multiple analyses, the flow condition in the entire depth range of the microfluidic chip was analyzed with improved scaling accuracy. The proposed method for flow profile construction and WSS calculation may be used for experimental measurements in biophysics and cellular biology studies, wherein a better understanding of the impact of mechanical shear stress is required. Although the developed codes are currently configured to work with the DefocusTracker algorithm, they can also be configured to work with any GDPT algorithm. The limitation of the proposed approach is that it is only applicable to the laminar flow condition and requires a flow rate that is sufficiently low for a video recording device to capture the motion of particles. The proposed method is only required for experimental setups that utilize basic biological laboratory equipment, i.e., using cell culture medium fluid or having no lens aberration.

SUPPLEMENTARY MATERIAL

The supplementary material provides detailed information of the processes described in the manuscript; the topics are PDMS microfluidic chip fabrication, calibration stack for Z axis depth estimation, and ImageJ-based cell counting analysis.

ACKNOWLEDGMENTS

This study was supported by Chulabhorn Royal Academy [fundamental fund: fiscal year 2023 by National Science Research and Innovation Fund (FRB660044/0240; Project code No. 180851)]. The authors express their sincere gratitude to the Synchrotron Light Research Institute, Thailand, for the provision of facilities and assistance in chip design and fabrication and to Miss Sirilak Phetcharat for her invaluable support to this study. We thank Edanz for editing a draft of this manuscript.

AUTHOR DECLARATIONS

Conflict of Interest

The authors have no conflicts to disclose.

Author Contributions

Hein Htet Aung and Phattarin Pothipan contributed equally to this paper.

Hein Htet Aung: Conceptualization (equal); Formal analysis (equal); Investigation (equal); Methodology (equal); Writing – original draft (lead); Writing – review & editing (lead). **Phattarin Pothipan:** Formal analysis (equal); Investigation (equal); Writing – original draft (equal); Writing – review & editing (equal). **Jirasin Aswakool:** Conceptualization (equal); Methodology (equal). **Siraphob Santironnarong:** Formal analysis (equal); Investigation (equal); Writing – original draft (equal); Writing – review & editing (equal). **Rungrueang Phatthanakun:** Funding acquisition (equal); Resources (equal); Supervision (equal). **Visarute Pinrod:** Resources (supporting). **Thanakorn Jiemsakul:** Resources (supporting). **Wares Chancharoen:** Conceptualization (equal); Funding acquisition (equal); Methodology (equal); Resources (equal); Supervision (equal). **Aekkacha Moonwiriyakit:** Funding acquisition (equal); Resources (equal); Supervision (equal).

DATA AVAILABILITY

The data that support the findings of this study are openly available in figshare repository at http://doi.org/10.6084/m9.figshare.25998874. Additional data, such as the raw video files and calibration images used in the DefocusTracker analysis, are available upon request. The codes associated with the proposed method are available in a repository at https://gitlab.com/aiim1/combine_DefocusTrack, along with a sample raw data generated from the DefocusTracker analysis of the experiment.

APPENDIX A: MESH SENSITIVITY COMPUTATIONAL FLUID DYNAMICS

The unstructured mesh was used for mesh generation, owing to its inherent capability of accommodating complex geometries. Several meshes were created and run at a flow rate of 20 μl/min. The WSS at the cross sections of different regions was probed to observe the convergence. Figure 10 illustrates the microfluidic computational domain and its fine numerical mesh. Table III summarizes the mesh elements for each mesh and WSS at a ROI.

As presented in Table III, the minimum grid points required to achieve mesh independence exceed 223 405. To minimize computational resources, further analysis should be based on this grid density. Therefore, the numerical evaluation result will be based on a grid with 1 467 673 points.

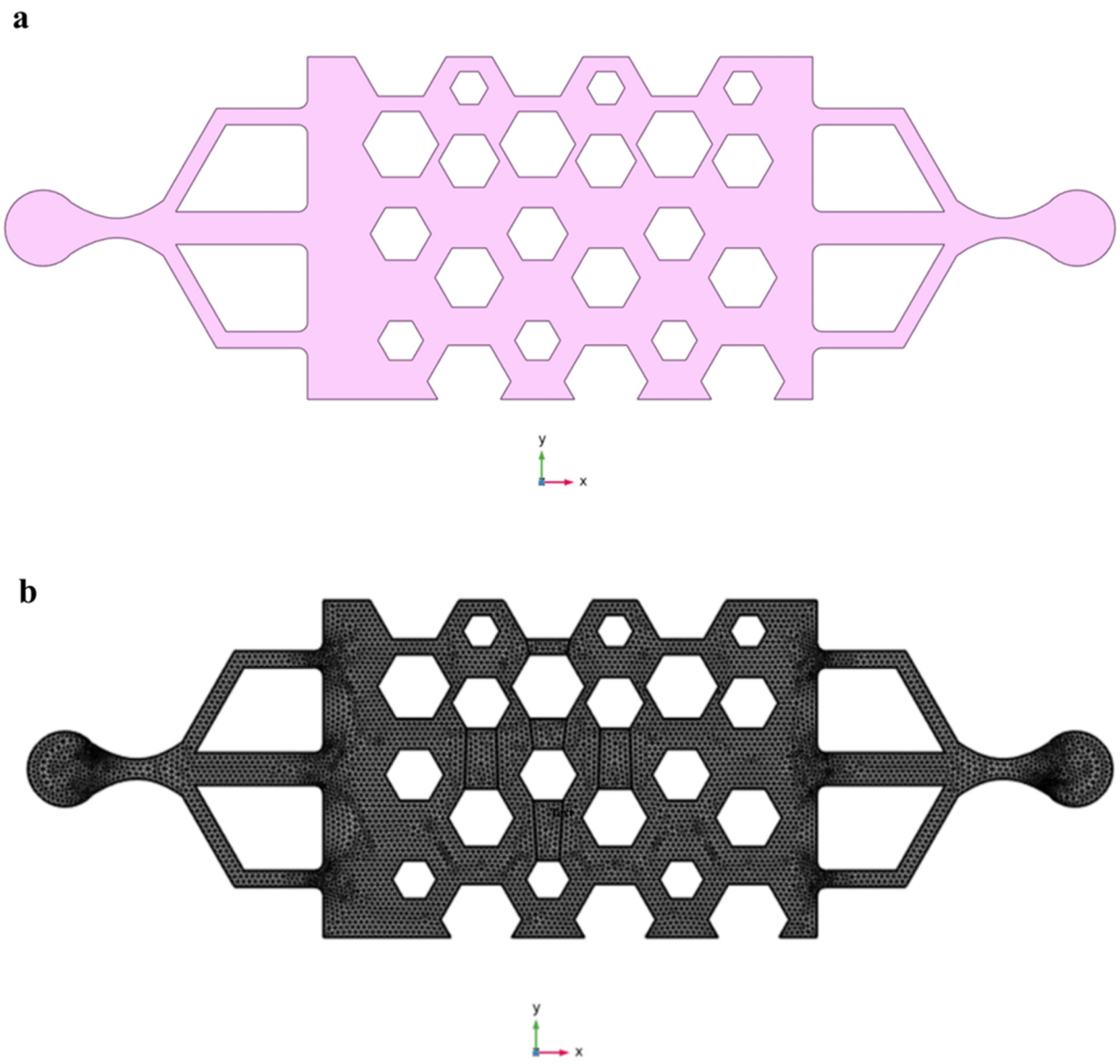

FIG. 10. (a) CAD model of microfluidic chip and (b) its computational grid.

TABLE III. WSS at different regions with respect to total grid points.

Total grid points	WSS at small-upstream (mPa)	WSS at medium-upstream (mPa)	WSS at large-upstream (mPa)
26 608	196.1	172.4	97.8
98 374	202.8	168.2	95.7
223 405	81.3	67.0	38.2
1 467 673	79.5	63.2	36.7

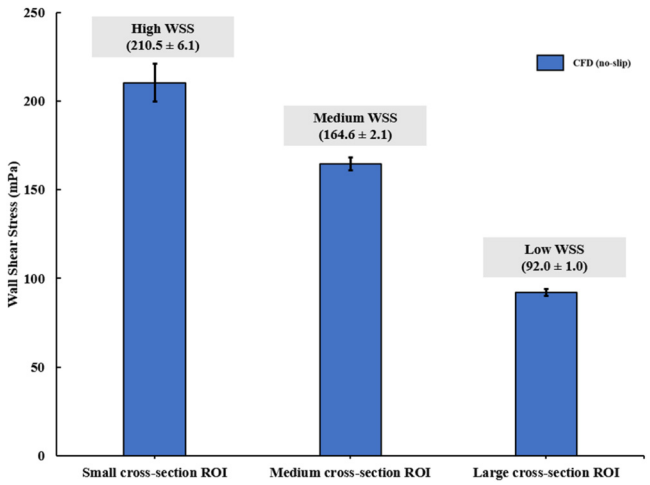

FIG. 11. Wall shear stress values at a flow rate of 50 μl/min obtained from CFD analysis.

APPENDIX B: WSS VALUES AT FLOW RATE OF 50 μl/min

The WSS at a flow rate of 50 μl/min was investigated by CFD analysis with the no-slip condition. The WSS levels vary depending on the channel width. The intensity of the WSS in ROIs with a small, medium, and large cross section was 211, 165, and 92, respectively. Therefore, the WSS is categorized into three groups: low WSS (92 mPa), medium WSS (165 mPa), and high WSS (211 mPa), as shown in Fig. 11.

REFERENCES

[1]S. Halldorsson, E. Lucumi, R. Gómez-Sjöberg, and R. M. T. Fleming, "Advantages and challenges of microfluidic cell culture in polydimethylsiloxane devices," Biosens. Bioelectron. **63**, 218–231 (2015).
[2]K. Matuła, F. Rivello, and W. T. S. Huck, "Single-cell analysis using droplet microfluidics," Adv. Biosyst. **4**(1), 1900188 (2020).
[3]H. Hino, M. Ochiai, S. Hashimoto, K. Kimura, and Y. Takahashi, "Effect of wall shear stress in flow on myoblast," in *Proceedings of the 19th World Multi-Conference on Systemics, Cybernetics and Informatics (WMSCI)* (2015), Vol. 2, pp. 246–251.
[4]H. Bahmaee, R. Owen, L. Boyle, C. M. Perrault, A. A. Garcia-Granada, G. C. Reilly, and F. Claeyssens, "Design and evaluation of an osteogenesis-on-a-chip microfluidic device incorporating 3D cell culture," Front. Bioeng. Biotechnol. **8**, 557111 (2020).
[5]E. Leclerc, B. David, L. Griscom, B. Lepioufle, T. Fujii, P. Layrolle, and C. Legallaisa, "Study of osteoblastic cells in a microfluidic environment," Biomaterials **27**(4), 586–595 (2006).
[6]W. Yu, H. Qu, G. Hu, Q. Zhang, K. Song, H. Guan, T. Liu, and J. Qin, "A microfluidic-based multi-shear device for investigating the effects of low fluid-induced stresses on osteoblasts," PLoS One **9**(2), e89966 (2014).
[7]X. Liu, X. Zhang, and I. Lee, "A quantitative study on morphological responses of osteoblastic cells to fluid shear stress," Acta Biochim. Biophys. Sin. **42**(3), 195–201 (2010).
[8]J. Rubin, C. Rubin, and C. R. Jacobs, "Molecular pathways mediating mechanical signaling in bone," Gene **367**, 1–16 (2006).
[9]F. M. Pavalko, N. X. Chen, C. H. Turner, D. B. Burr, S. Atkinson, Y.-F. Hsieh, J. Qiu, and R. L. Duncan, "Fluid shear-induced mechanical signaling in MC3T3-E1 osteoblasts requires cytoskeleton-integrin interactions," Am. J. Physiol. Cell Physiol. **275**(6), C1591–C1601 (1998).
[10]Y. Ban, Y. Wu, T. Yu, N. Geng, Y. Wang, X. Liu, and P. Gong, "Response of osteoblasts to low fluid shear stress is time dependent," Tissue Cell **43**(5), 311–317 (2011).
[11]D. C. Genetos, D. J. Geist, D. Liu, H. J. Donahue, and R. L. Duncan, "Fluid shear-induced ATP secretion mediates prostaglandin release in MC3T3-E1 osteoblasts," J. Bone Miner. Res. **20**(1), 41–49 (2005).
[12]G. C. Buscaglia and R. F. Ausas, "Variational formulations for surface tension, capillarity and wetting," Comput. Methods Appl. Mech. Eng. **200**(45–46), 3011–3025 (2011).
[13]V. Majarikar, H. Takehara, and T. Ichiki, "Adsorption phenomena of anionic and cationic nanoliposomes on the surface of poly(dimethylsiloxane) microchannel," J. Photopolym. Sci. Technol. **32**(1), 107–113 (2019).
[14]G. M. Whitesides, "The origins and the future of microfluidics," Nature **442**(7101), 368–373 (2006).
[15]J. G. Santiago, S. T. Wereley, C. D. Meinhart, D. J. Beebe, and R. J. Adrian, "A particle image velocimetry system for microfluidics," Exp. Fluids **25**(4), 316–319 (1998).
[16]R. J. Adrian, "Particle-imaging techniques for experimental fluid mechanics," Annu. Rev. Fluid Mech. **23**(1), 261–304 (1991).
[17]P. F. Salipante, "Microfluidic techniques for mechanical measurements of biological samples," Biophys. Rev. **4**(1), 011303 (2023).
[18]S. Zhou, B. Chen, E. S. Fu, and H. Yan, "Computer vision meets microfluidics: A label-free method for high-throughput cell analysis," Microsyst. Nanoeng. **9**(1), 116 (2023).
[19]H. Varçin, F. Üneş, E. Gemici, and M. Zelenakova, "Development of a three-dimensional CFD model and OpenCV code by comparing with experimental data for spillway model studies," Water **15**(4), 756 (2023).
[20]M. H. Qureshi, W.-H. Tien, and Y.-J. P. Lin, "Performance comparison of particle tracking velocimetry (PTV) and particle image velocimetry (PIV) with long-exposure particle streaks," Meas. Sci. Technol. **32**(2), 024008 (2021).
[21]R. Barnkob and M. Rossi, "*DefocusTracker*: A modular toolbox for defocusing-based, single-camera, 3D particle tracking," J. Open Res. Softw. **9**(1), 22 (2021).
[22]S. J. Rao, S. Sharma, S. Basu, and C. Tropea, "Depth from defocus technique: A simple calibration-free approach for dispersion size measurement," Exp. Fluids **65**(4), 55 (2024).
[23]C. Cierpka, R. Segura, R. Hain, and C. J. Kähler, "A simple single camera 3C3D velocity measurement technique without errors due to depth of correlation and spatial averaging for microfluidics," Meas. Sci. Technol. **21**(4), 045401 (2010).
[24]E. Lammertse, N. Koditala, M. Sauzade, H. Li, Q. Li, L. Anis, J. Kong, and E. Brouzes, "Widely accessible method for 3D microflow mapping at high spatial and temporal resolutions," Microsyst. Nanoeng. **8**(1), 72 (2022).
[25]W. Chancharoen, J. Aswakool, H. H. Aung, S. Phetcharat, P. Pothipan, A. Moonwiriyakit, R. Phatthanakkun, and T. Jiemsakul, "In-situ and near-real time of shear stress measurement of multiple shear stress lab-on-chip for osteoblast cell cultivation using image analysis," in *TSME International Conference on Mechanical Engineering (ICoME 2023)* (Chiang Mai, Thailand, December 2023), pp. 383–392.
[26]F. Zhao, D. Lacroix, K. Ito, B. Van Rietbergen, and S. Hofmann, "Changes in scaffold porosity during bone tissue engineering in perfusion bioreactors considerably affect cellular mechanical stimulation for mineralization," Bone Rep. **12**, 100265 (2020).
[27]M.-S. Chun, T. S. Lee, and K. Lee, "Microflow of dilute colloidal suspension in narrow channel of microfluidic-chip under Newtonian fluid slip condition," Korea Aust. Rheol. J. **17**(4), 207–215 (2005).
[28]I. Tirelli, A. Ianiro, and S. Discetti, "A simple trick to improve the accuracy of PIV/PTV data," Experimental Therm. Fluid Sci. **145**, 110872 (2023).
[29]M. Rossi and R. Barnkob, "A fast and robust algorithm for general defocusing particle tracking," Meas. Sci. Technol. **32**(1), 014001 (2020).
[30]B. E. Rapp, "Conservation of mass: The continuity equation," in *Microfluidics: Modelling, Mechanics, and Mathematics* (Elsevier, 2017), pp. 265–271.

[31]Z. Cai, N. Chattopadhyay, W. J. Liu, C. Chan, J.-P. Pignol, and R. M. Reilly, "Optimized digital counting colonies of clonogenic assays using ImageJ software and customized macros: Comparison with manual counting," Int. J. Radiat. Biol. **87**(11), 1135–1146 (2011).
[32]T. Cross, R. Navarange, J.-H. Son, W. Burr, A. Singh, K. Zhang, M. Rusu, K. Gkoutzis, A. Osborne, and B. Nieuwenhuis, "Simple RGC: ImageJ plugins for counting retinal ganglion cells and determining the transduction efficiency of viral vectors in retinal wholemounts," J. Open Res. Softw. **9**(1), 15 (2021).
[33]H. Polzer, F. Haasters, W. C. Prall, M. M. Saller, E. Volkmer, I. Drosse, W. Mutschler, and M. Schieker, "Quantification of fluorescence intensity of labeled human mesenchymal stem cells and cell counting of unlabeled cells in phase-contrast imaging: An open-source-based algorithm," Tissue Eng. Part C Methods **16**(6), 1277–1285 (2010).
[34]C. Karmonik, O. Diaz, R. Klucznik, R. G. Grossman, Y. J. Zhang, G. Britz, N. Lv, and Q. Huang, "Quantitative comparison of hemodynamic parameters from steady and transient CFD simulations in cerebral aneurysms with focus on the aneurysm ostium," J. Neurointerv. Surg. **7**(5), 367–372 (2015).
[35]I. C. Campbell, J. Ries, S. S. Dhawan, A. A. Quyyumi, W. R. Taylor, and J. N. Oshinski, "Effect of inlet velocity profiles on patient-specific computational fluid dynamics simulations of the carotid bifurcation," J. Biomech. Eng. **134**(5), 051001 (2012).
[36]X. Wang, J. He, H. Wang, D. Zhao, B. Geng, S. Wang, J. An, C. Wang, H. Han, and Y. Xia, "Fluid shear stress regulates osteoblast proliferation and apoptosis via the lncRNA TUG1/miR-34a/FGFR1 axis," J. Cell. Mol. Med. **25**(18), 8734–8747 (2021).
[37]P. Malaviya and R. M. Nerem, "Fluid-induced shear stress stimulates chondrocyte proliferation partially mediated via TGF-β 1," Tissue Eng. **8**(4), 581–590 (2002).
[38]R. C. Riddle, A. F. Taylor, D. C. Genetos, and H. J. Donahue, "MAP kinase and calcium signaling mediate fluid flow-induced human mesenchymal stem cell proliferation," Am. J. Physiol. Cell Physiol. **290**(3), C776–C784 (2006).
[39]S. Weinbaum, S. C. Cowin, and Y. Zeng, "A model for the excitation of osteocytes by mechanical loading-induced bone fluid shear stresses," J. Biomech. **27**(3), 339–360 (1994).